Micromodel observations of evaporative drying and salt deposition in porous media

Ayorinde Rufai, and John Crawshaw

Citation: Physics of Fluids **29**, 126603 (2017);
View online: https://doi.org/10.1063/1.5004246
View Table of Contents: http://aip.scitation.org/toc/phf/29/12
Published by the American Institute of Physics



Micromodel observations of evaporative drying and salt deposition in porous media

Ayorinde Rufai[1,2] and John Crawshaw[1,2,a)]
[1]*Department of Chemical Engineering, Imperial College London, London SW7 2AZ, United Kingdom*
[2]*Qatar Carbonates and Carbon Storage Research Centre, Imperial College London, London SW7 2AZ, United Kingdom*

(Received 12 September 2017; accepted 8 December 2017; published online 29 December 2017)

Most evaporation experiments using artificial porous media have focused on single capillaries or sand packs. We have carried out, for the first time, evaporation studies on a 2.5D micromodel based on a thin section of a sucrosic dolomite rock. This allowed direct visual observation of pore-scale processes in a network of pores. NaCl solutions from 0 wt. % (de-ionized water) to 36 wt. % (saturated brine) were evaporated by passing dry air through a channel in front of the micromodel matrix. For de-ionized water, we observed the three classical periods of evaporation: the constant rate period (CRP) in which liquid remains connected to the matrix surface, the falling rate period, and the receding front period, in which the capillary connection is broken and water transport becomes dominated by vapour diffusion. However, when brine was dried in the micromodel, we observed that the length of the CRP decreased with increasing brine concentration and became almost non-existent for the saturated brine. In the experiments with brine, the mass lost by evaporation became linear with the square root of time after the short CRP. However, this is unlikely to be due to capillary disconnection from the surface of the matrix, as salt crystals continued to be deposited in the channel above the matrix. We propose that this is due to salt deposition at the matrix surface progressively impeding hydraulic connectivity to the evaporating surface. *Published by AIP Publishing.* https://doi.org/10.1063/1.5004246

I. INTRODUCTION

Drying of a porous medium is an important process that has motivated many studies; its applications are vast including environmental and industrial applications such as groundwater and soil remediation, food processing, and preservation, and geological applications such as carbon sequestration and the recovery of hydrocarbons from underground reservoirs. Two boundary conditions are common; first, if dry gas is injected into the pore space, it will displace the liquid already saturating the matrix away from the injection surface simultaneously with evaporation;[1] second, if dry gas passes across the face of a porous medium as it would for a surface soil or in gas injection into a fractured formation, the evaporation flux is orthogonal to the main gas flow.[2] We will discuss the second process. In this case, the drying process is characterised by the stepwise gas phase invasion of an initially liquid saturated porous medium. This leads to the formation of a drying front defined as an interface separating the liquid saturated and partially gas-filled domains.[2] Evaporative drying from a porous medium can also be seen as an immiscible displacement process in which a viscous wetting phase (brine) is replaced by a less viscous nonwetting phase (gas) in the pore space.[3] Despite the extensive literature available on the drying process, accurate predictions of the evaporative drying rate and a comprehensive description of the different stages involved in drying are still major challenges, particularly when drying is combined with the deposition of salt.

Generally, three stages of the evaporation of pure water in a porous medium have been clearly described: initially, at high liquid saturation, there is an early stage with a high and relatively constant evaporation rate (stage-1) followed by a falling and much lower evaporation rate (stage-2).[2–6] These stages are connected by a crossover period characterised by a significant drop in evaporative drying rate.[4] In some literature, the stage-2 period and the crossover period are described as one period; however, these periods are often classically referred to in sequential order as the constant rate period (CRP), falling rate period (FRP), and receding front period (RFP).[5] The kinetics of these periods depend on the combination of external and internal mass transfers during the drying process.[4] During the first period, liquid water is still present at the external surface of the matrix and the drying rate is dependent on the external mass transfer to the vapour phase. Dry gas entering the pores to balance the loss of liquid becomes rapidly saturated with water vapour, so little evaporation occurs inside the porous medium. The drying rate during this period is constant (or at least pseudo-constant),

$$\frac{dx}{dt} \alpha\ K. \tag{1}$$

By integrating Eq. (1), we have $x\ \alpha\ t$. Hence, evaporation varies linearly with time during the CRP. During the later stages when the region close to the surface becomes dry, the internal mass transfer limits the drying rate, and diffusion of water vapour is the dominant process,

a)Author to whom correspondence should be addressed: j.crawshaw@imperial.ac.uk

$$\frac{dx}{dt}\alpha\ x. \tag{2}$$

By integrating,

$$\int x dx = \int dt, \tag{3}$$

and then

$$x^2\alpha\ t. \tag{4}$$

The drying rate varies linearly with the square root or time during the later stages of evaporation. In simpler terms, evaporative drying rates in porous media are affected by the temperature, surface area, humidity, and velocity of drying air (all external mass transfers) and vapour diffusion, thermal and hydraulic conductivities, and pore space geometry (internal mass transfers).

The dynamic interplay of these factors leads to complex interactions between transport processes, boundary conditions, atmospheric conditions, and media properties which consequently results in a complex and sometimes ambiguous range of evaporation behaviors.[2,5,7] At the onset of evaporative drying, the evaporative demand imposed by atmospheric conditions is balanced by capillarity, i.e., liquid flow through wetting films connecting the evaporative surface to the receding drying front.[2,6,8,9] However, the liquid connections to the drying surface cannot be maintained for long; as the liquid saturation in the region below the drying surface reduces and the size of this region increases, the connecting liquid pathways can no longer provide sufficient flow and capillarity is overcome by viscous (and gravity) effects. This marks the beginning of the receding front period. The motivation for this study was to investigate the impact of salt deposition on this process.

Sub-surface porous media (saline aquifers, oil and gas reservoirs, etc.) naturally contain dissolved mineral salts. Others have salt trapped in them, for instance, salts get trapped in masonry materials during acid rain.[10] The crystallisation/dissolution cycles these salts undergo cause significant damage to the porous building materials used in civil engineering.[11–19] Salt crystallisation in porous media also causes a significant decrease in permeability of underground reservoirs. This decrease in permeability leads to reduced injectivity and possibly storage potential in CO_2 sequestration and reduced oil and gas production from hydrocarbon reservoirs.[20]

In addition to the studies on the drying of pure water from porous media, a number of publications address salt crystallisation during evaporation of water from brine in porous media. These studies looked at a variety of factors affecting crystallization in porous media such as wettability,[21,22] 1D systems,[15,23–26] 2D systems,[22,25] relative humidity,[27] heterogeneity of the porous media,[28–30] and the effect of confined systems.[19,31,32] The distribution (crusty or patchy)[10,21,28,29] and the position (surface salt, efflorescence, or salt precipitation within the matrix, sub-florescence) of the precipitated salt have also been observed.[9,18,21] However, a good understanding of the effects of the salt and its deposited crystals on the different stages of water evaporation in porous media is imperative to mitigate the aforementioned problems caused by salt precipitation.

Lastly, the geometry of a porous medium is often very complex, and in order to understand more clearly what takes place, we must begin by looking at very simple patterns, from which some qualitative deductions can be made.[33] Studies on individual capillaries have been shown to be a very important step in gaining more insight into understanding the transport processes in porous media.[4,34–36] The evaporation from a capillary bundle, the next simple model of porous media, has also been studied.[36] There are a number of evaporation studies in the literature using micromodels[22,37–40] including very recent ones.[41,42] These previous studies have used different methods of injecting the dry gas that provides the driving force for evaporation, depending on the application of the research. Some[37] have chosen to inject directly into the matrix, producing a simultaneous drainage displacement and evaporation process appropriate to the near well-bore dry-out occurring during CO_2 storage in an unfractured reservoir or saline aquifer. Others[22,38–42] flow the drying gas past the outside of the micromodel allowing evaporation through a region of "stagnant air" where diffusion controls the maximum evaporation rate, a process representative of the drying of a soil at the surface of the earth. In this study, we have chosen to continuously flow dry air through a channel adjacent the matrix, thereby maintaining a very low relative humidity at the exposed edge of the matrix throughout the drying process. This is the boundary condition appropriate for what happens in a fractured reservoir when dry CO_2 is being injected for carbon storage processes. Therefore, our micromodels were designed to have (fracture) channels on each side of the matrix, and the flow rate of dry gas was carefully chosen to maintain a humidity close to zero in the channel while preventing forced advection into the matrix. Choices also need to be made about the geometry of the matrix region of the model, and while the previous studies discussed earlier use synthetic arrays of either capillaries or pillar obstacles, in this study, we have decided to use micromodels based on a thin section of sucrosic dolomite, a natural carbonate rock. This study will also be of interest in the increasingly popular field of microfluidics.[34,43]

The use of micromodels allows the visualization pore scale events in real time using direct imaging and optical microscopy. This is of great advantage as a direct visualisation of transport processes at the pore scale in real porous media is very challenging requiring the use of complex computed tomography scanners. These scanners, however, cannot provide real time visualization.[44,45] Hence, the use of optically transparent micromodels offers an attractive alternative for real time visualization (imaging) at the pore scale. Also, since micromodels are synthetic systems, they offer an added advantage of flexibility. The micromodels can be designed (user has a major control on model's wettability, geometry, roughness, and so on) to address very specific research questions. In Sec. II, the characterization of the micromodels used for this study will be presented in more detail.

II. METHOD DEVELOPMENT

A. Micromodels

Micromodels are 2.5D pore networks that allow direct visualization of flows in them through a microscope or other visual imaging technique. The micromodels used in this study are based on thin-section images of a sucrosic dolomite rock as

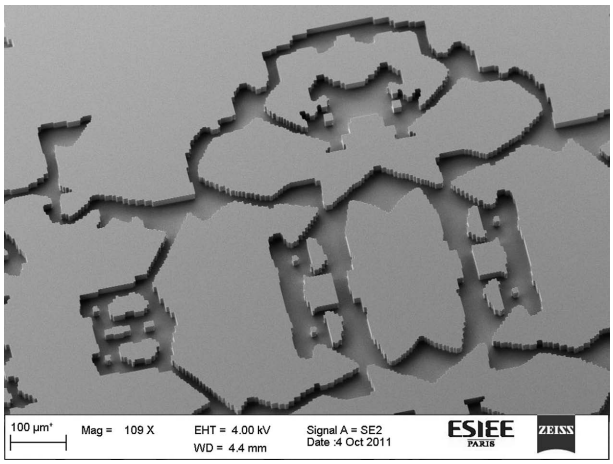


FIG. 1. An SEM image of the sucrosic dolomite micromodel wafer.

an example of a simple carbonate structure. The pattern designs were derived from existing rock section images as pioneered by Hornbrook[46] and Rangel-German and Kovscek.[47] The micromodels were fabricated from silicon wafers with a glass cover, allowing precise control of the channel geometry and hence a good representation of the original rock thin section. The fabrication procedure follows the procedure pioneered by Ref. 46. A Scanning Electron Microscope (SEM) image of a section of the etched micromodel wafer is shown in Fig. 1.

Fluid injection and production are through the ports (highlighted with red circles in Fig. 2) connected to the ducts that run along the two open edges of the micromodel matrix. These ducts allow one edge of the matrix to be maintained at a low humidity to induce evaporation (representing a fracture in real rock structures). They also allow fluids to flow in and out of the model during the initial saturation. The model matrix size is 2.5×1 cm^2 etched area with a constant etch depth of 25 μm. The duct width at each end is 500 μm, and the matrix grain size ranges between 6 and 1250 μm. The average porosity measured from the binarized model image was estimated to be 0.28, and the total pore area (excluding vertical channels) is approximately 0.7 cm^2. The coordination number varied between 1 and 4, with matrix permeability of about 350 mD. The etched silicon surface of the micromodel was oxidised to ensure that it is water wet before bonding the glass plate onto the silicon wafer to create an isolated flow path. This was done by heating the silicon wafer on a hotplate at about 315 °C for 1 h. The high air temperature oxidizes the silicon by forming a silicon oxide film, which is water wetting. The oxidation was done during fabrication at École Supérieure d'Ingénieurs en Électrotechnique et Électronique [ESIEE (Paris)].

B. Imaging techniques

The results and images presented in this study were acquired by optical imaging techniques. A DSLR (digital single lens reflex) camera (D800E, Nikon) combined with a macro-lens (AF-S Micro Nikkor 105 mm, Nikon) and filter (Pro1 Digital Close-Up No. 3, Hoya) was used to capture images that require a wide field of view and rapid image acquisition. For continuous operation, instead of a conventional battery, an AC adapter (EH-5b, Nikon) was connected to the camera via a power connector (EP-5B, Nikon). Snapshots and videos can be recorded with the DSLR; it can also be set to take images at set time intervals. The camera was linked to the personal computer (PC) via a universal serial bus (USB) cable that allows the camera to be controlled remotely via dedicated software: Camera Control Pro 2 (version 2.13.0, Nikon).

For high-resolution imaging of the micromodel, an inverted light microscope (ILM) (AxioObserver A1.m, Zeiss) was used. A motorized stage (Mac 6000 system Ludl Electronic Products Ltd.) was incorporated into the ILM; this allows for accurate positioning of the micromodels. The ILM was equipped with a number of objectives ranging from 2.5× to 50× magnification providing high-quality images from which precise dimensions of the micro-model channel, pore, and throat widths can be measured. Images are captured by a digital camera (AxioCam HSc) attached to the left side port of the microscope; live images of the model positioned on the stage can be viewed through either the eyepiece or directly on the PC by running specialist software AxioVision (Version 4.8.1, Zeiss) attached to the microscope via a FireWire cable.

C. Experimental procedure

All experiments were conducted at ambient temperature. Fresh NaCl brine solutions ranging in concentration from 0 wt. % to 36 wt. % (saturated) were prepared as required for this study. Fluorescein (46960-25G-F, Sigma-Aldrich. 1:700 000 v/v) dye was added to the brine solution for easier phase differentiation. The brine was injected into the micromodel with a 10 ml syringe (BD Plasipak, BD300013) using a programmable syringe pump (BS-80000, Braintree Scientific Ltd.). The experimental setup with the inverted light microscope system is shown in Fig. 3(a). The micromodel holder designed and fabricated in-house was used to position the model with the injection and production ports.

Initially, 100% brine saturation of the micromodel could not be achieved due to the presence of trapped air bubbles.

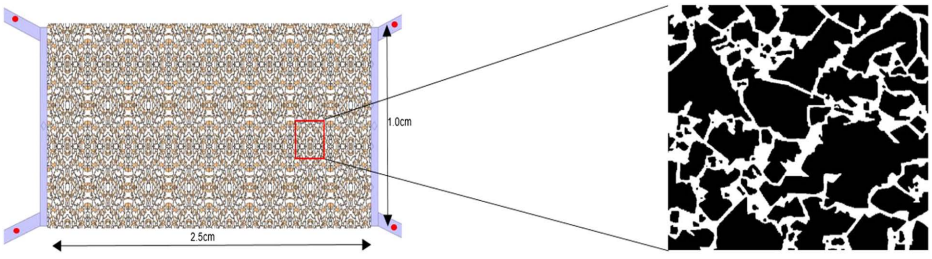
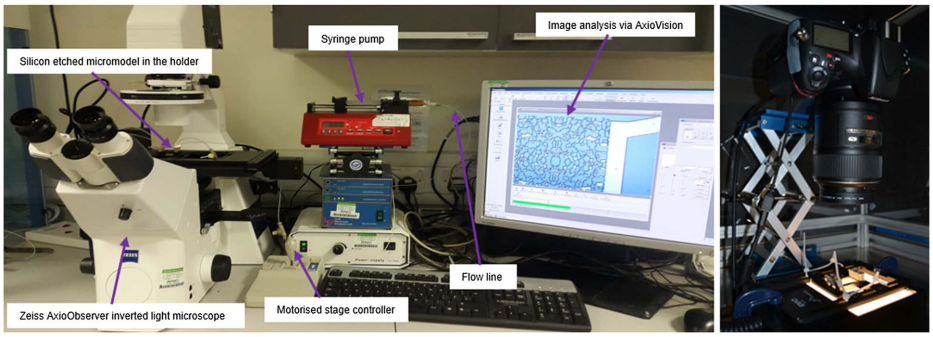


FIG. 2. Micromodel dimension with the repeated pattern shown as an inset.



(a) (b)

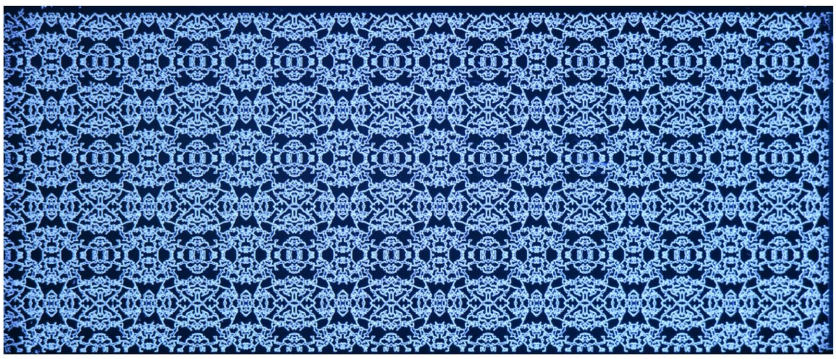
FIG. 3. The experimental setup with the (a) ILM and (b) DSLR.

To mitigate against this, at the start of the experiment, the dry micromodel was flushed with CO_2 to displace the air before brine injection. This allowed 100% brine saturation of the model to be achieved due to the solubility of CO_2 in brine. After ensuring model saturation by microscopic inspection, the valves at the four ports were closed and the imaging technique was changed to the DSLR system to obtain images of the entire micro-model matrix. The DSLR camera was positioned on an adjustable stand, constructed in-house, facing vertically downwards onto the micromodel which was positioned horizontally to eliminate any gravity effects [Fig. 3(b)]. The camera was linked to a personal computer via a USB cable allowing it to be controlled remotely via dedicated software: Camera Control Pro 2 (version 2.13.0, Nikon).

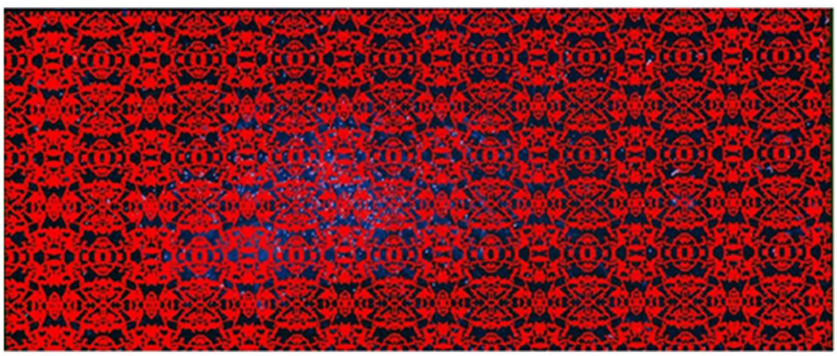
The two ports on the duct at the side of the matrix chosen for evaporation were then opened: one to a dry compressed air line and the other to the atmosphere to allow the flow of air out of the model. The compressed air pressure was set at 0.5 bar which resulted in an air flow rate of approximately 0.3 ml/s. The air flow-rate was carefully chosen to avoid forced advection into the matrix while at the same time to maintain the very low humidity boundary conditions in the channel. The drying pattern, the movement of the evaporating front into the matrix and the salt deposition left in its wake, was imaged at different time intervals until complete dry-out. The microvisual data thus obtained were processed and quantitatively analyzed as described in Sec. II D.

D. Image processing

The raw images captured with the DSLR camera were saved in the Tagged Image File Format (TIFF) format (without compression) to preserve important image qualities and properties. Extracting quantitative data from the images requires some image processing. This was done with ImageJ, an open source software. The images were initially cropped and registered before image segmentation. First, the foreground colour was set to white and the background to black before setting the measurements needed, for example, area, perimeter, and



(a)



(b)

FIG. 4. (a) Raw image of a micromodel saturated with dyed brine, cropped to show only the matrix. (b) Segmented image of a micromodel saturated with brine (measured area is covered in red in ImageJ).

area fraction and so on. The images were opened in 24-bit red-green-blue (RGB) format in ImageJ; spatial calibrations were done by scaling the pixel size to an appropriate unit of length (μm) using the known size of the micromodel pattern. The threshold colour plugin was then used to segment the dry pores for subsequent area measurement. Examples of the image segmentation are given below.

Figure 4(a) is a raw image of the micromodel at zero liquid saturation, i.e., full of gas and empty of any liquid taken with the DSLR camera setup before drying starts; the white regions represent empty pore areas, while the deep blue regions represent the micromodel solid "grains." Figure 4(b) is the result of segmenting Fig. 4(a) using ImageJ with the procedure highlighted earlier; the empty pore regions are now red in colour, while the solid "grain" remains the same colour. Similarly, Fig. 5(a) is a raw image of the micromodel taken sometime during dry-out; the greenish yellow regions represent pore areas saturated with dyed water (or brine); the white regions represent pore areas that are completely dry; the light blue regions are pore areas empty of liquid but still with liquid films at the corners, while the deep blue regions represent the micromodel solid "grains." Figure 5(b) is the result of segmenting Fig. 5(a); regions still with liquid phase remain greenish yellow; dry regions (including dry regions with liquid corner films) are now red in colour, while the solid "grain" remains the same colour.

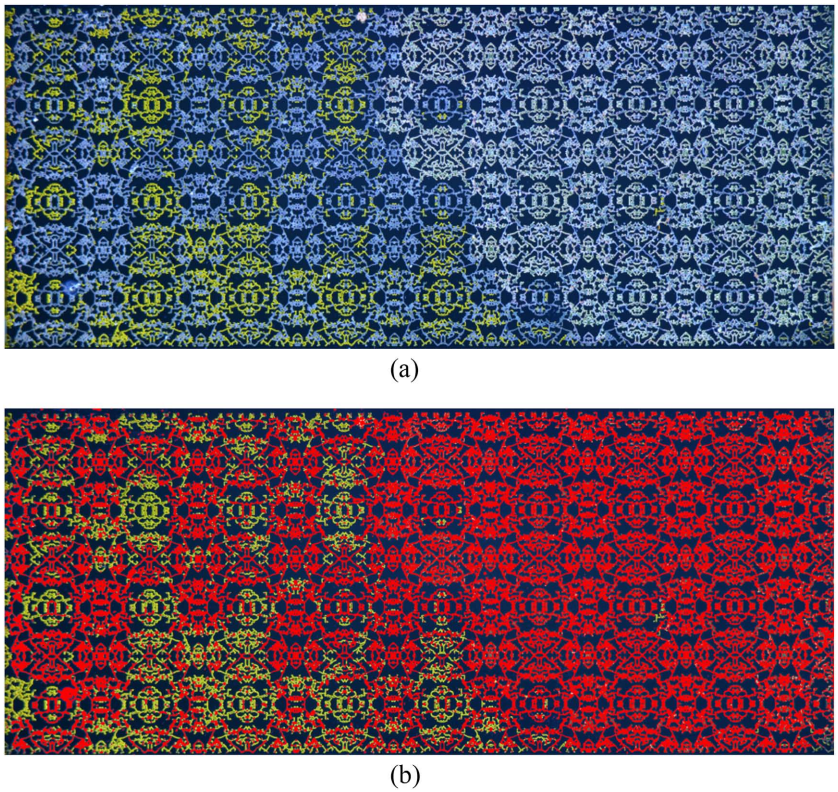
Unfortunately, the pore area containing precipitated salt could not be accurately segmented separately from the dry pore area due to insufficient contrast. Also, a simple mass balance on the brine (the total volume of the salt in the micro-model was calculated before and after dry-out) shows that the salt deposition does not completely fill the entire depth (25 μm) of the micro-model throughout the matrix. This means that there are regions where the pores and throats are only partially blocked after salt deposition. The quantitative data presented in this study are subject to uncertainty in dry pore area measurements. This has been estimated to be ± 0.02 cm^2 from repeated experiments and measurements.

III. RESULTS AND DISCUSSION

A. Evolution of drying in a water-wet micromodel

During drying, the area of the pores occupied by gas/vapour (equivalent to mass lost by evaporation) was estimated by image analysis as shown earlier. Figures 6(a) and 6(b) show the dry pore area as a function of time for different brine concentrations. Three different periods can be seen from the plot of each of the brine concentration. The slope of each of the plot indicates their respective evaporation rates. The rate of evaporation at early times was pseudo-constant for all the brine concentrations measured. This was followed by a transition period, eventually leading to a late time evaporation period with a much lower slope. For de-ionized water (0 wt. % NaCl), these three periods correspond to the classical periods of evaporation expected from earlier experiments and modeling in porous media drying: the constant rate period (CRP) in which liquid remains connected to the drying surface, the falling rate period (FRP) or transition period, and the receding front period (RFP), in which the capillary connection is broken and water transport becomes dominated by vapour diffusion.[1–5,48–50]

For the different brine concentrations (12 wt. %–36 wt. % NaCl brine), we observed the same trend although the



(a)

(b)

FIG. 5. (a) Raw image of a micromodel during drying. (b) Segmented image of a micromodel during drying brine (measured area is covered in red in ImageJ).

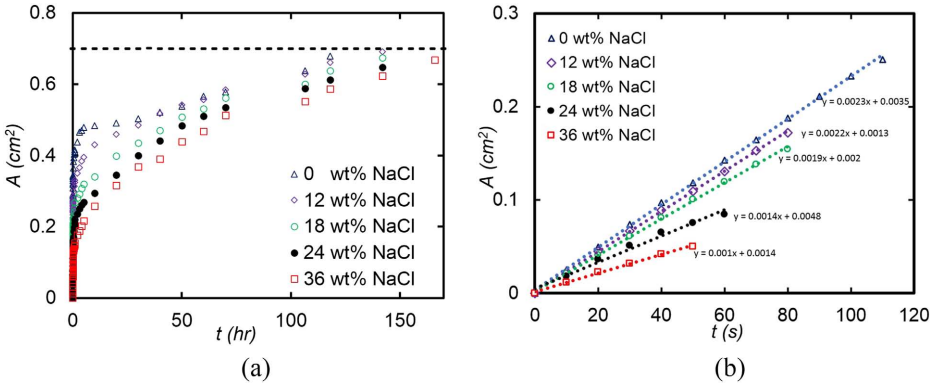


FIG. 6. Evolution of drying: (a) dry pore area as a function of time (horizontal black dotted line shows the total pore dry area = 0.7 cm^2) and (b) early time dry pore area as a function of time.

transition from the CRP occurred systematically earlier and at higher liquid saturations as the initial brine concentration was increased. The evaporation rates for the brine solutions during the CRP are lower than that of de-ionized water; this is expected from the reduction of water vapour pressure in the presence of dissolved ions: the equilibrium vapour pressure above de-ionized water is 2.49 kPa, significantly higher than 1.88 kPa for saturated brine solution.[51] The observation that the CRP (for de-ionized water) is actually a period of slowly reducing evaporation rate in porous media drying was first put forward over three decades ago.[5] However, in this study, the evaporation rate of de-ionized water was seen to remain constant during the initial period.

According to our vapour pressure theory, the evaporation rate of the different salt concentrations should all become the same just before salt deposition. This is not the case seen in Fig. 6(b); the slopes of the CRP decrease with increasing initial salt concentration. To normalize the CRP, we scaled the slopes by the vapour pressures of their corresponding salt concentration as illustrated in Table I. The slope/vapour pressure for the different salt concentrations is of the same order and approximately the same for 0 wt. %, 12 wt. %, and 18 wt. % NaCl brines. The slight difference in the slope/vapour pressure of the 24 wt. % and 36 wt. % NaCl brines may be attributed to salt deposited at the early time acting as a physical barrier to the liquid phase connectivity.

B. Different stages of evaporation during porous media drying

The three periods of evaporation are best illustrated in Fig. 7(a), which shows the drying curve as a plot of evaporation rate E (normalised by maximum evaporation rate, E_{max}) as a function of liquid saturation, S. The evaporation rate E is estimated from $\delta A/\delta t$. The liquid saturation is defined as $S = (A_{max} - A)/A_{max}$; this has been computed to follow the same convention as for real porous medium drying curve. A_{max} is the total pore area which is equal to the pore dry area after complete dry-out. The assumptions made in generating these parameters are as follows:

1. We have neglected possible wetting films still connected to the evaporative surface from the drying front. The dry areas are assumed to be completely dry without any remaining liquid at the corners.
2. Liquid filled pore areas are assumed to be completely saturated (this might not be accurate as we can only view the 25 μm silicon depth in one direction from above).
3. We have assumed that water density is uniform and neglected gravity effects.

Figure 7(a) gives a clearer picture of the three periods of drying. For de-ionized water, we observed the three classical periods of evaporation expected: the CRP, FRP, and RFP. The transition from the CRP is at the time (or saturation) at which the drying rate ceases to be almost constant, while the transition from FRP to RFP is marked by the time (or saturation) at which the evaporation rate becomes linear in the square root of time.

For the brines, we observed that the length of the CRP decreased with increasing brine concentration and became almost non-existent for 36 wt. % NaCl solution (saturated brine). In the experiments with brine, the dry area of the matrix became linear with the square root of time [Fig. 7(b)] after the short CRP. However, this is unlikely to be due to capillary disconnection from the surface of the matrix as is usually the case for de-ionized water drying,[4] as the salt crystals continued to be deposited almost exclusively in the duct at the edge of the matrix as seen in the time sequence images in Fig. 8. We therefore contend that the onset of the square root of time drying for brines should not be associated with a receding evaporation front, as is the case for de-ionized water, as the liquid brine must remain connected to the outer surface of the matrix through corner wetting films for salt to be deposited there. For brine systems, the square root of time behavior started almost immediately after the start of drying (especially for the saturated brine). Therefore, we speculate that the development of dry solid salt patches in the fracture and matrix close

TABLE I. Slopes of the CRP as a function of vapour pressure for the different NaCl brine concentrations.

Salt concentration (wt. %)	Evaporation rate (cm^2/min)	Vapour pressure (KPa)	$\frac{\text{Rate}\,(\frac{cm^2}{min})}{\text{Vapour pressure (KPa)}}$
0	0.0023	3.170	7.3×10^{-4}
12	0.0022	3.091	7.1×10^{-4}
18	0.0019	2.650	6.8×10^{-4}
24	0.0014	2.518	5.6×10^{-4}
36	0.0010	2.401	4.2×10^{-4}

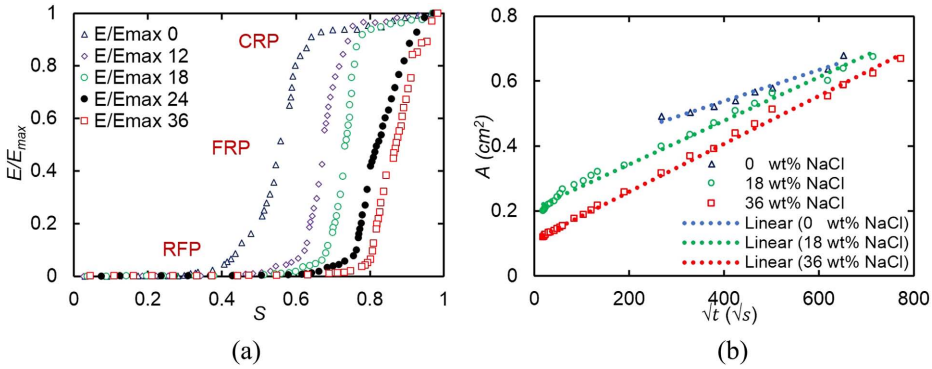


FIG. 7. Evolution of drying: (a) evaporation as a function of liquid saturation and (b) dry pore area as a function of square root of time.

to the fracture (plugging the pores and throats) and the relatively high viscosity of saturated NaCl brine (compared to de-ionized water) which will provide a higher viscous resistance to mass transfer (liquid flow) are possible causes for the square root of time behavior. Eventually the hydraulic connectivity to the evaporating surface is broken, and the salt concentration deep inside the matrix increases until the solubility limit is exceeded, resulting in solid salt deposition within the matrix.

C. Combined evaporation and salt precipitation

Evaporation in brine systems is accompanied by salt precipitation. As water is evaporated from the solution, the brine concentration increases until it exceeds the solubility limit, leading to the deposition of solid salt crystals.[52,53] The achievable degree of supersaturation may depend on the porous media, and there is some evidence from studies in glass capillaries that higher supersaturation can be attained in confinement.[31,32] Figure 9 provides visual evidence for salt precipitation mainly in the evaporating surface and in some pores just below it for a water-wet micromodel. The grayish dark particles in each of the images are precipitated salt in the evaporating surface (fracture) and in the matrix near the evaporating surface. Figure 9(b) is a zoomed-in image of the matrix showing a blocked pore.

For saturated brine, we expect the evaporation rate to remain relatively high (although lower than that of de-ionized water because of the decrease in vapour pressure) since the deposited salt crystals have a similar wettability to that of the clean micromodel. Tests on single NaCl crystals showed that the saturated brine spreads on the dry salt surface. Capillary continuity is maintained for a significant time into the experiment. However, the reverse is what we observe: the evaporation rate falls sharply as soon as drying starts, and we believe this is due to the appearance of dry patches above the deposited salt at the evaporating surface, thereby reducing the surface area available for evaporation.

From Fig. 7(b), we see that the drying curve for the 36 wt. % NaCl brine (saturated brine) goes into the square

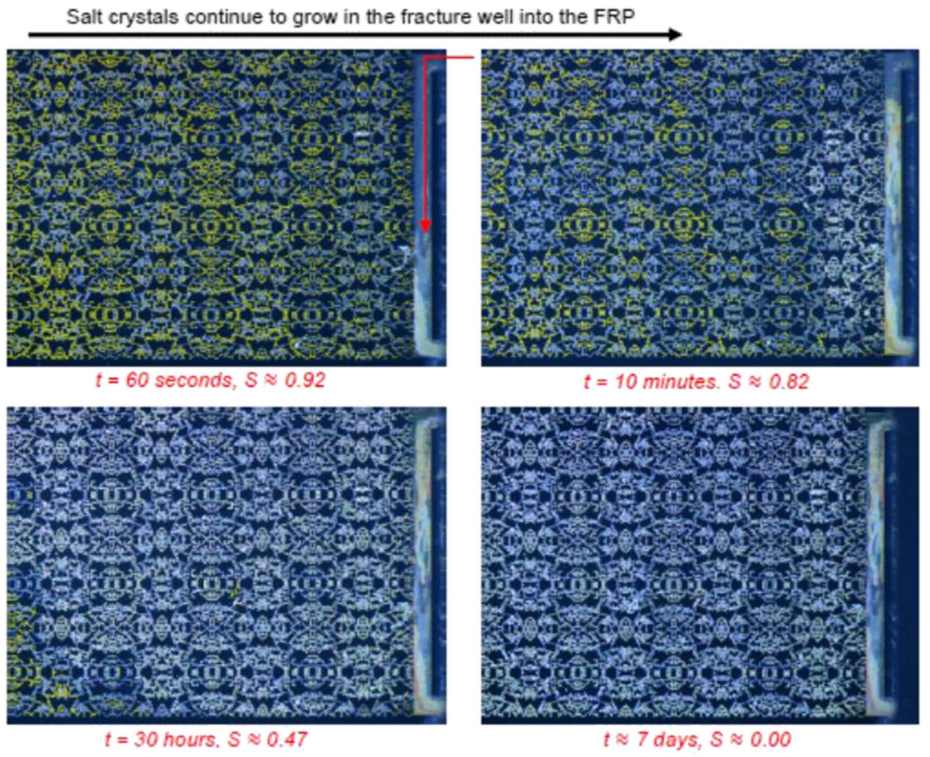


FIG. 8. Evolution of salt deposit at the fracture for initial salt concentration of 36 wt. % NaCl brine at different times during dry-out (the greenish yellow regions represent pore areas saturated with dyed brine; the white and light blue regions represent pore areas that are dry, while the deep blue regions represent the micromodel solid "grains." Salt can be seen growing continuously in the fracture and in the matrix close to the fracture). The red arrow shows the direction of air flow into the fracture.

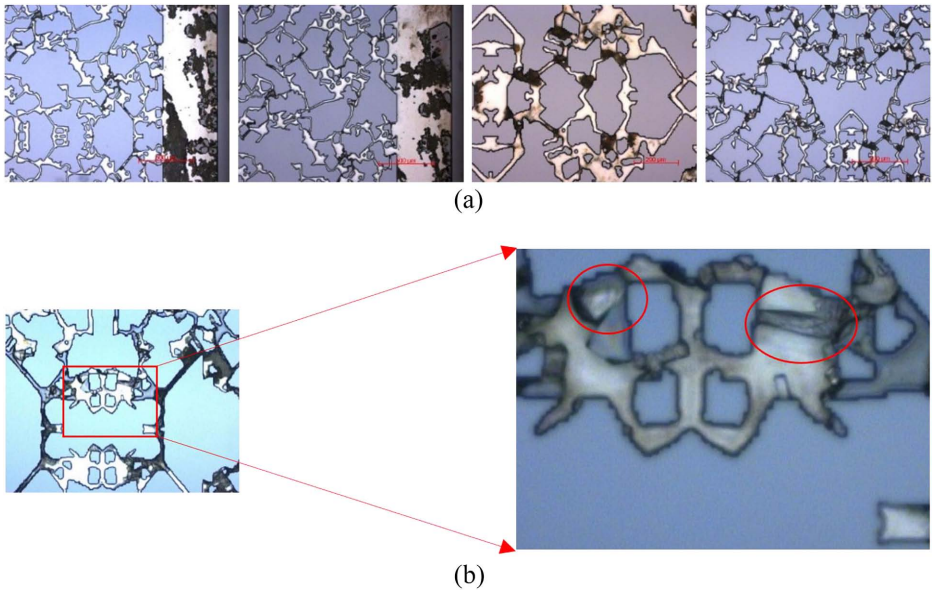


FIG. 9. (a) Images showing deposited salt in the evaporating surface and in the matrix below at the end of complete drying (i.e., liquid saturation, S = 0). (b) The zoomed-in image of a pore body blocked by deposited salt. The red-O rings highlight crystals blocking pore throats and bodies. The high-resolution images were taken with the inverted light microscope.

root of time ($\sqrt{t}$) regime almost immediately as drying starts. The reason for this immediate transition into the vapour diffusion limited period for saturated brine is likely due to the deposition of salt (which starts almost immediately with drying at this brine concentration) greatly impeding liquid flow to the evaporating surface as seen in Figs. 9(a) and 9(b). The higher viscosity of the saturated brine also makes the viscous resistance to liquid flow greater. All these combine to make the evaporation rate fall as soon as drying starts.

As stated earlier, liquid transport takes place at the evaporating surface through capillarity. Theoretical evidence for this is provided by Refs. 25 and 26. This leads to the accumulation of salt at the evaporating surface. As drying continues, there is a gradual increase in brine concentration at the evaporating surface until it becomes precipitated as solid salt. This effect is counterbalanced by the Fickian diffusion process that tends to homogenise the salt profile.[45] Hence, we estimated the Peclet number, *Pe*, at the high and low evaporation rates for the saturated brine experiment using the following equation:

$$Pe = \frac{EL}{W\phi D}. \tag{5}$$

E is the evaporation rate (estimated as the pore dry area per unit length and unit time in cm^2/s), L is the length of the micromodel in cm, W is the width of matrix in cm, ϕ is the model porosity, and D is the diffusion coefficient in cm^2/s. For high Peclet numbers ($Pe \gg 1$), the salt accumulates at the evaporating surface, while for low Peclet numbers, diffusion dominates and the deposited salt profile is homogeneous and spreads out in the matrix. From our experiment, the Peclet number for the high evaporation rate period for 36 wt. % NaCl solution was calculated to be about 260 at ambient conditions, confirming that the advection pulls the brine to the evaporating surface much faster than diffusion could spread dissolved salt in the opposite direction in the matrix. However, for the low evaporation rate [from a liquid saturation of about 0.8 from Fig. 7(a)], the Peclet number was calculated to be about 10. This is still greater than 1 but much lower than the value for the high evaporation rate period. Therefore, we suggest that diffusion has become relatively stronger and could in fact spread high concentration dissolved salt to some degree against the evaporative flux in the matrix.

D. Permeability alteration in porous media as a consequence of salt deposition during drying

During the injection of CO_2 in underground reservoirs, solid salt is precipitated as a result of convective drying (and/or a strong water desaturation) of the residual brine in the reservoir. A sizeable amount of the salt is deposited in the fracture, while some are deposited in the matrix close to the fracture. This often leads to a decrease in porosity, permeability, and the overall storage potential of the reservoir. It also leads to increase in injection pressure and the overall cost of the process. We have studied the permeability alteration due to salt precipitation induced by drying for our micromodels.

We have done this in two ways: first considering the fracture permeability and then the matrix permeability. The two permeabilities were measured after complete drying by injecting air at a known flow rate and measuring the resulting pressure drop first through the matrix and then only through the duct carrying the dry air during the evaporation stage of the experiment. The results are plotted in Fig. 10. We observed two regions [highlighted with red and blue trend lines in Figs. 10(a) and 10(b)] of a linear downward trend in the matrix and fracture permeability measurements: first with 0 wt. %–18 wt. % before a sharp decrease and another downward trend from the 24 wt. % to the 36 wt. % brine. Overall, the matrix permeability, fracture permeability, and permeability alteration all decreases with increasing brine concentration and is almost total for the saturated brine concentration (36 wt. % brine or 360 g/l brine).

Also, we defined permeability alteration as the ratio of final permeability to initial permeability[54] and plotted it as a

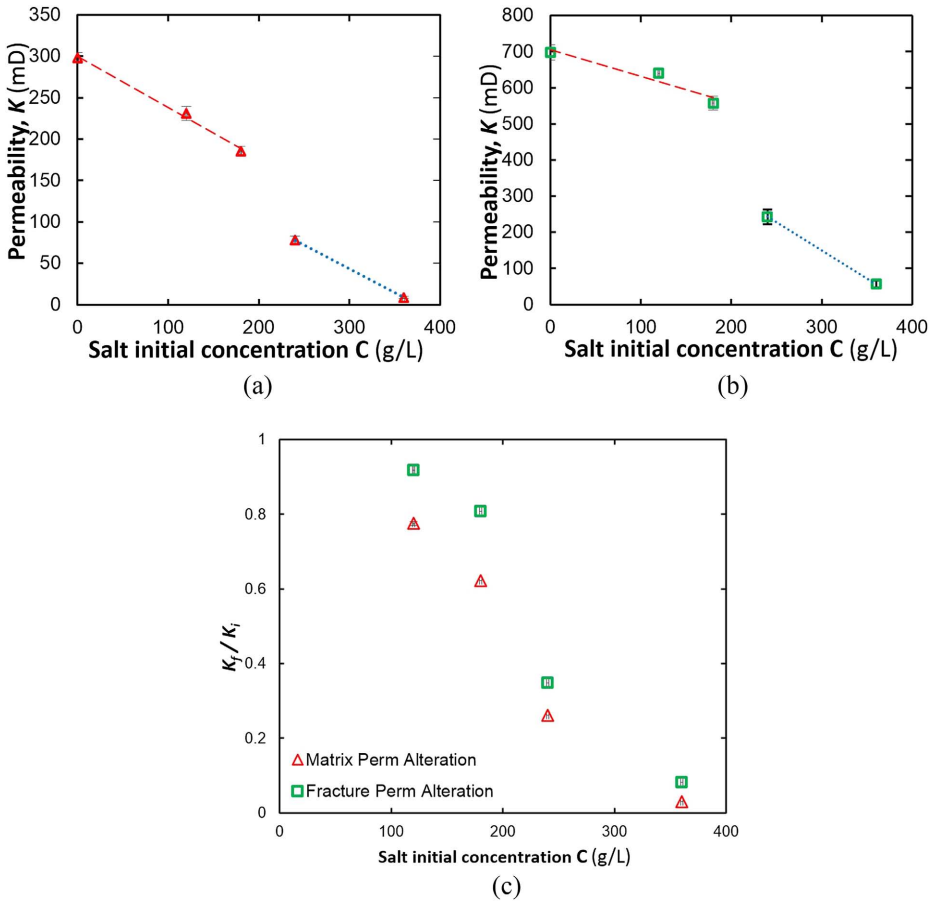


FIG. 10. Permeability versus initial salt concentration for the micromodel (a) matrix and (b) fracture. (c) Permeability alteration versus initial salt concentration for the matrix and fracture.

function of brine concentration for the fracture and matrix as plotted in Fig. 10(c).

IV. CONCLUSIONS

The rate of drying has been measured for de-ionized water in a micromodel based on a thin section image of a sucrosic dolomite rock. The evaporation rate followed the well-established constant rate period at an early time and then a transition to a lower rate becoming linear in the square root of time as the capillary connection to the drying surface was broken and diffusion of water vapour through dry pores started to dominate.

Drying curves were also measured in the same micromodel for NaCl brine at a range of initial concentrations up to saturation. The shape of the drying curve was superficially similar to that of water but with a shorter CRP. However, in this case, the break from the constant evaporation rate is not simply related to liquid depinning from the external surface of the pore space as it occurs sooner and the wettability of the deposited salt (water wet) is similar to that of the micromodel surfaces. Deposition of salt crystals appears to block liquid paths to the evaporating surface and may lead to the development of dry patches at the surface of the pore space. After a short transition, the brine drying curves were all linear when plotted as the square root of time.

The extent of permeability damage measured after complete drying depended systematically on the initial brine concentration for both the matrix and the duct representing a fracture at the face of the matrix.

ACKNOWLEDGMENTS

We gratefully acknowledge funding from the Petroleum Technology Development Fund (PTDF), provided by the Nigerian Government through the Presidential Special Nigeria Scholarship Scheme for Innovation and Development (PRESSID). We also gratefully acknowledge the equipment used for this research provided by the Qatar Carbonates and Carbon Storage Research Centre (QCCSRC), funded jointly by Qatar Petroleum, Shell, and Qatar Science and Technology Park.

[1]H. Ott, S. M. Roels, and K. de Kloe, "Salt precipitation due to supercritical gas injection: I. Capillary-driven flow in unimodal sandstone," Int. J. Greenhouse Gas Control **43**, 247–255 (2015).
[2]P. Lehmann, S. Assouline, and D. Or, "Characteristic lengths affecting evaporative drying of porous media," Phys. Rev. E **77**(5), 056309 (2008).
[3]N. Shokri, P. Lehmann, and D. Or, "Liquid-phase continuity and solute concentration dynamics during evaporation from porous media: Pore-scale processes near vaporization surface," Phys. Rev. E **81**(4), 046308 (2010).
[4]F. Chauvet, P. Duru, S. Geoffroy, and M. Prat, "Three periods of drying of a single square capillary tube," Phys. Rev. Lett. **103**(12), 124502 (2009).
[5]J. Van Brakel, "Mass transfer in convective drying," Adv. Drying **1**, 217–267 (1980).
[6]G. W. Scherer, "Theory of drying," J. Am. Ceram. Soc. **73**(1), 3–14 (1990).
[7]M. Prat, "Recent advances in pore-scale models for drying of porous media," Chem. Eng. J. **86**(1), 153–164 (2002).
[8]A. Yiotis, A. Stubos, A. Boudouvis, I. Tsimpanogiannis, and Y. Yortsos, "Pore-network modeling of isothermal drying in porous media," Transp. Porous Media **58**(1), 63–86 (2005).

[9]N. Shokri, P. Lehmann, and D. Or, "Critical evaluation of enhancement factors for vapor transport through unsaturated porous media," Water Resour. Res. **45**(10), W10433, https://doi.org/10.1029/2009wr007769 (2009).
[10]N. Shahidzadeh-Bonn, S. Rafaï, D. Bonn, and G. Wegdam, "Salt crystallization during evaporation: Impact of interfacial properties," Langmuir **24**(16), 8599–8605 (2008).
[11]C. Rodriguez-Navarro and E. Doehne, "Salt weathering: Influence of evaporation rate, supersaturation and crystallization pattern," Earth Surf. Processes Landforms **24**(3), 191–209 (1999).
[12]D. Everett, "The thermodynamics of frost damage to porous solids," Trans. Faraday Soc. **57**, 1541–1551 (1961).
[13]A. Goudie and H. A. Viles, *Salt Weathering Hazard* (Wiley, 1997).
[14]G. W. Scherer, "Stress from crystallization of salt," Cem. Concr. Res. **34**(9), 1613–1624 (2004).
[15]H. Huinink, L. Pel, and M. A. J. Michels, "How ions distribute in a drying porous medium: A simple model," Phys. Fluids **14**(4), 1389–1395 (2002).
[16]M. Steiger, "Crystal growth in porous materials—I: The crystallization pressure of large crystals," J. Cryst. Growth **282**(3), 455–469 (2005).
[17]N. Shahidzadeh-Bonn, J. Desarnaud, F. Bertrand, X. Chateau, and D. Bonn, "Damage in porous media due to salt crystallization," Phys. Rev. E **81**(6), 066110 (2010).
[18]V. N. Wong, R. C. Dalal, and R. S. Greene, "Salinity and sodicity effects on respiration and microbial biomass of soil," Biol. Fertil. Soils **44**(7), 943–953 (2008).
[19]J. Desarnaud, H. Derluyn, L. Molari, S. de Miranda, V. Cnudde, and N. Shahidzadeh, "Drying of salt contaminated porous media: Effect of primary and secondary nucleation," J. Appl. Phys. **118**(11), 114901 (2015).
[20]N. Muller, R. Qi, E. Mackie, K. Pruess, and M. J. Blunt, "CO2 injection impairment due to halite precipitation," Energy Procedia **1**(1), 3507–3514 (2009).
[21]M. Bergstad and N. Shokri, "Evaporation of NaCl solution from porous media with mixed wettability," Geophys. Res. Lett. **43**(9), 4426–4432, https://doi.org/10.1002/2016gl068665 (2016).
[22]H. Eloukabi, N. Sghaier, M. Prat, and S. Ben Nassrallah, "Drying experiments in a hydrophobic model porous medium in the presence of a dissolved salt," Chem. Eng. Technol. **34**(7), 1085–1094 (2011).
[23]H. Eloukabi, N. Sghaier, S. B. Nasrallah, and M. Prat, "Experimental study of the effect of sodium chloride on drying of porous media: The crusty–patchy efflorescence transition," Int. J. Heat Mass Transfer **56**(1), 80–93 (2013).
[24]S. Veran-Tissoires, M. Marcoux, and M. Prat, "Discrete salt crystallization at the surface of a porous medium," Phys. Rev. Lett. **108**(5), 054502 (2012).
[25]N. Sghaier and M. Prat, "Effect of efflorescence formation on drying kinetics of porous media," Transp. Porous Media **80**(3), 441–454 (2009).
[26]L. Guglielmini, A. Gontcharov, A. J. Aldykiewicz, Jr., and H. A. Stone, "Drying of salt solutions in porous materials: Intermediate-time dynamics and efflorescence," Phys. Fluids **20**(7), 077101 (2008).
[27]S. Gupta, H. P. Huinink, M. Prat, L. Pel, and K. Kopinga, "Paradoxical drying of a fired-clay brick due to salt crystallization," Chem. Eng. Sci. **109**, 204–211 (2014).
[28]S. Veran-Tissoires and M. Prat, "Evaporation of a sodium chloride solution from a saturated porous medium with efflorescence formation," J. Fluid Mech. **749**, 701–749 (2014).
[29]F. Hidri, N. Sghaier, H. Eloukabi, M. Prat, and S. B. Nasrallah, "Porous medium coffee ring effect and other factors affecting the first crystallisation time of sodium chloride at the surface of a drying porous medium," Phys. Fluids **25**(12), 127101 (2013).
[30]U. Nachshon, N. Weisbrod, M. I. Dragila, and A. Grader, "Combined evaporation and salt precipitation in homogeneous and heterogeneous porous media," Water Resour. Res. **47**(3), W03513, https://doi.org/10.1029/2010wr009677 (2011).
[31]A. Naillon, P. Duru, M. Marcoux, and M. Prat, "Evaporation with sodium chloride crystallization in a capillary tube," J. Cryst. Growth **422**, 52–61 (2015).
[32]J. Desarnaud, H. Derluyn, J. Carmeliet, D. Bonn, and N. Shahidzadeh, "Metastability limit for the nucleation of NaCl crystals in confinement," J. Phys. Chem. Lett. **5**(5), 890–895 (2014).
[33]C. Marle, *Multiphase Flow in Porous Media* (Éditions TECHNIP, 1981).
[34]T. M. Squires and S. R. Quake, "Microfluidics: Fluid physics at the nanoliter scale," Rev. Mod. Phys. **77**(3), 977 (2005).
[35]J. Stefan, "On the equilibrium and movement of gas mixtures, in particular diffusion," Sitzungsber. Kais. Akad. Wiss. Wien **63**, 63–124 (1871).
[36]B. Camassel, N. Sghaier, M. Prat, and S. B. Nasrallah, "Evaporation in a capillary tube of square cross-section: Application to ion transport," Chem. Eng. Sci. **60**(3), 815–826 (2005).
[37]M. Kim, A. Sell, and D. Sinton, "Aquifer-on-a-chip: Understanding pore-scale salt precipitation dynamics during CO2 sequestration," Lab Chip **13**(13), 2508–2518 (2013).
[38]N. Vorhauer, Y. Wang, A. Kharaghani, E. Tsotsas, and M. Prat, "Drying with formation of capillary rings in a model porous medium," Transp. Porous Media **110**(2), 197–223 (2015).
[39]J. B. Laurindo and M. Prat, "Numerical and experimental network study of evaporation in capillary porous media. Drying rates," Chem. Eng. Sci. **53**(12), 2257–2269 (1998).
[40]J. B. Laurindo and M. Prat, "Numerical and experimental network study of evaporation in capillary porous media. Phase distributions," Chem. Eng. Sci. **51**(23), 5171–5185 (1996).
[41]C. Chen, P. Duru, P. Joseph, S. Geoffroy, and M. Prat, "Control of evaporation by geometry in capillary structures. From confined pillar arrays in a gap radial gradient to phyllotaxy-inspired geometry," Sci. Rep. **7**(1), 15110 (2017).
[42]P. Fantinel, O. Borgman, R. Holtzman, and L. Goehring, "Drying in a microfluidic chip: Experiments and simulations," Sci. Rep. **7**(1), 15572 (2017).
[43]G. Karniadakis and A. Beskok, *Micro Flows: Fundamentals and Simulation* (Springer Verlag, New York, NY, 2002).
[44]P. van Hemert, E. S. J. Rudolph, and P. L. Zitha, "Micro computer tomography study of potassium iodide precipitation in Bentheimer sandstone caused by flow-through CO2 drying," Energy Procedia **37**, 3331–3346 (2013).
[45]S. M. Roels, H. Ott, and P. L. Zitha, "μ-CT analysis and numerical simulation of drying effects of CO2 injection into brine-saturated porous media," Int. J. Greenhouse Gas Control **27**, 146–154 (2014).
[46]J. Hornbrook, L. Castanier, and P. Pettit, "Observation of foam/oil interactions in a new, high-resolution micromodel," in *SPE Annual Technical Conference and Exhibition* (Society of Petroleum Engineers, 1991).
[47]E. Rangel-German and A. Kovscek, "A micromodel investigation of two-phase matrix-fracture transfer mechanisms," Water Resour. Res. **42**(3), W03401, https://doi.org/10.1029/2004wr003918 (2006).
[48]N. Shahidzadeh-Bonn, A. Azouni, and P. Coussot, "Effect of wetting properties on the kinetics of drying of porous media," J. Phys.: Condens. Matter **19**(11), 112101 (2007).
[49]M. Prat, "On the influence of pore shape, contact angle and film flows on drying of capillary porous media," Int. J. Heat Mass Transfer **50**(7), 1455–1468 (2007).
[50]A. Yiotis, A. Boudouvis, A. Stubos, I. Tsimpanogiannis, and Y. Yortsos, "Effect of liquid films on the drying of porous media," AIChE J. **50**(11), 2721–2737 (2004).
[51]R. Robinson, "The vapour pressures of solutions of potassium chloride and sodium chloride," Trans. R. Soc. N. Z. **75**(2), 203–217 (1945).
[52]G. Bacci, A. Korre, and S. Durucan, "Experimental investigation into salt precipitation during CO2 injection in saline aquifers," Energy Procedia **4**, 4450–4456 (2011).
[53]Y. Wang, E. Mackie, J. Rohan, T. Luce, R. Knabe, and M. Appel, "Experimental study on halite precipitation during CO2 sequestration," in *International Symposium of the Society of Core Analysts Held in Noordwijk, The Netherlands* (The Society of Core Analysts, 2009), pp. 27–30.
[54]Y. Peysson, B. Bazin, C. Magnier, E. Kohler, and S. Youssef, "Permeability alteration due to salt precipitation driven by drying in the context of CO2 injection," Energy Procedia **4**, 4387–4394 (2011).